High Resolution Spectroscopy with XMM

Frits Paerels, A. C. Brinkman, J. W. den Herder, C. de Vries, A. J. F. den Boggende,
R. Mewe, J. Kaastra

Space Research Organization of the Netherlands,
Sorbonnelaan 2, 3584 CA Utrecht, the Netherlands

Steven M. Kahn, Andrew P. Rasmussen, Todd Decker, Marcela Stern,
Jean Cottam, Joshua Spodek

Columbia Astrophysics Laboratory, Columbia University,
538 West 120th Street, New York NY10027, USA

Graziella Branduardi-Raymont

Mullard Space Science Laboratory,
Holmbury St Mary, Dorking, Surrey, RH5 6NT, United Kingdom

Manuel Guedel

Paul Scherrer Institut, CH-5232 Villigen PSI, Switzerland

Duane A. Liedahl

Lawrence Livermore National Laboratory,
7000 East Ave., P.O. Box 808, Livermore, CA 94550, USA

Christian Erd

European Space Research and Technology Centre (ESTEC),
Space Science Department, Astrophysics Division,
Postbus 299, NL-2200 AG Noordwijk, the Netherlands

ABSTRACT

XMM is designed to provide sensitive, high resolution spectroscopy, on a wide variety of cosmic sources. We briefly review some issues related to high-resolution spectroscopy with the observatory, with emphasis on spectroscopy with the RGS. The most important spectroscopic plasma diagnostics accessible with the RGS are reviewed, after which we discuss possible approaches to qualititative and quantitative analysis of spectral datasets.

1. Introduction

With the launch of *AXAF*, *XMM*, and *Astro-E*, high resolution spectroscopy of a large number of sources of all varieties will become available. The potential of high resolution spectroscopy for

addressing a range of astrophysical questions unambiguously, and in detail, is obvious. But this observational potential will also change the way data is analyzed, and techniques and attitudes analogous to those in astrophysical spectroscopy in other wavelength bands will be introduced in X-ray astronomy. Before we discuss some of the specifics of high resolution spectroscopy with the Reflection Grating Spectrometers (RGS; see the contributions by Brinkman *et al.* and Rasmussen *et al.*, these proceedings), we will briefly consider the rationale for high resolution spectroscopy, because it provides a natural introduction to the rest of the discussion.

The simplest possible reason to study a high resolution spectrum, even if a rough characterization of the source characteristics (*e.g.* dominant line excitation mechanism, degree of equilibration, approximate electron temperatures, elemental abundance pattern, etc.) already exists from previous studies, is to check on the correctness of the spectral models employed. That this is not superfluous is shown by two examples drawn from recent research. The very first *ASCA* spectra of clusters revealed anomalous $(n = 4 \rightarrow 2)/(n = 3 \rightarrow 2)$ emission line ratio's in the Fe L ions, which impeded the unambiguous interpretation of the data (Fabian *et al.* 1994). The problem was traced to inaccuracies in the atomic data underlying the spectral models, and this situation has since been remedied with new, dedicated atomic structure and level population calculations (Liedahl *et al.* 1995). The second example concerns the Extreme ultraviolet spectra of coronae observed with *EUVE*. Here, it was found that emission line equivalent widths appear to be smaller than expected. A unique explanation for this effect cannot be given on the basis of the *EUVE* spectra alone. Currently viable explanations include abundance effects, resonance scattering and subsequent destruction of photons in partially optically thick lines, and the cumulative effect of numerous weaker lines missing from the spectral models, masquerading as continuum (Schrijver, van den Oord, and Mewe 1994; Mewe *et al.* 1995; Schmitt, Drake, and Stern 1996). Resolution of this problem will probably have to await higher sensitivity and wider bandwidth spectroscopy. These, and similar problems are most directly addressed with dedicated laboratory X-ray spectroscopy experiments coupled with modern calculations. An example of the power of this approach is given by the examination of the Fe XVII $n = n' \rightarrow 2$ spectrum by Brown *et al.* (1998, and references therein).

The most obvious rationale for high resolution spectroscopy is of course that it provides direct sensitivity to conditions in the source through microphysical diagnostics. In the next section, we will briefly review a few standard diagnostics that are accessible with the RGS. Finally, based on these diagnostics, a straightforward inspection of the spectrum should allow one to decide on the gross characteristics of the source: the dominant line excitation mechanism, issues of source homogeneity (evidence for a distribution of temperatures or ionization parameters, need to consider the superposition of physically distinct sources, like starburst regions and the immediate circumnuclear environment in Seyfert 2 galaxies, etc.), degree of equilibration, etc., before even attempting a gross fit with perhaps an inappropriate model.

2. Spectroscopic Diagnostics of Interest with the RGS

In the following, we discuss some standard spectroscopic diagnostics in the RGS band. Whether a particular physical effect can be detected and employed depends of course on signal-to-noise, among other things, but for the present discussion we will assume that a well-exposed spectrum exists, with a sufficiently large number of photons that discrete structure is significantly detected, and we concentrate on resolving power. That decouples this discussion to some extent from specific astrophysical assumptions and characteristics of particular sources, so that we can leave the astrophysical applications to your imagination.
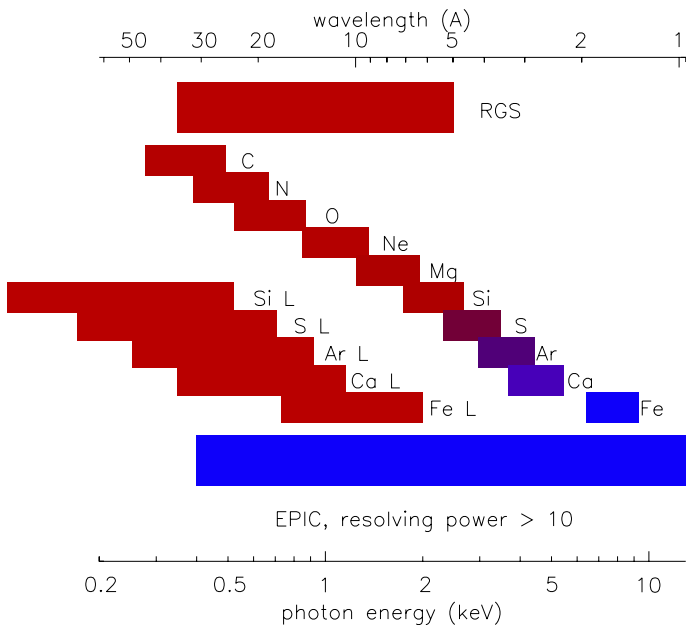

Fig. 1.— Schematic of the EPIC and first order RGS bandpasses, with the K and L bands of the abundant elements overlaid.

Figure 1 is a schematic of the (first order) RGS and EPIC bandpasses; for EPIC we show the band where the resolving power $\mathcal{R}$ of the instruments exceeds $\mathcal{R} > 10$, which is roughly what is needed to separate at least the H- and He-like charge states. Also indicated are the K-bands for the abundant elements C through Fe (between the energy of the $K\alpha$ transition in the neutral species and the ground state ionization energy of the Hydrogenic species), and the L-bands of the higher-Z elements (between the lowest-energy $n = 3 \rightarrow 2$ transition in the current line lists, and the ground state ionization energy of the Li-like species).

The RGS has resolution approximately $\Delta\lambda = 0.05$ Å (HEW; $\Delta\lambda = 0.08$ Å FWHM) in first order (See Brinkman *et al.*, these proceedings), while EPIC has $\Delta E \sim 50(E/1 \text{ keV})^{1/2}$ eV; this corresponds to resolving powers $\mathcal{R} \sim 300(\lambda/15 \text{ Å})$ for the RGS (first order), and $\mathcal{R} \sim 20(E/1 \text{ keV})^{1/2}$ for EPIC. The RGS band contains the bulk of the discrete K spectra for the elements C through Si, and the L spectra from Fe down to Si; of these L spectra, the Fe L

spectrum will ususally be by far the brightest. The considerable overlap between the spectra for all these elements again indicates the need for high spectral resolution, in order to avoid confusion (we will come back to this issue in Section 3). In addition to these more or less familiar spectra, other features may also appear, *e.g.* the Balmer spectrum of H-like Fe and the analogous spectrum from He-like Fe, lines from less abundant elements, etc. We now discuss some specific diagnostics.

Charge State Distribution At the lowest level is the ability to separate individual charge states of the elements. The charge state distribution is a strong diagnostic of the ionization balance, and the plasma parameters on which it depends. To distinguish the strongest $n = 2 \rightarrow 1$ transitions in the H- and He-like ions requires resolving power $\mathcal{R} \sim Z$ (with Z the nuclear charge), so $\mathcal{R} \sim 6 - 26$. Similar resolving power is required to uniquely identify absorption edges.

Charge State Spectroscopy: near-Neutral Species, and Fluorescence Spectroscopy To distinguish the near-neutral charge states by the energies of their fluorescent Kα lines is considerably harder. For oxygen, removal of the first valence electron increases the energy of the Kα line by about 6 eV; for neon through argon, the increment is about $14 - 17$ eV (Kaastra and Mewe 1993). To see these effects therefore requires resolving power $\mathcal{R} \sim 100 - 200$. However, to uniqely separate the Fe Kα lines in the various Fe M-shell ions requires up to $\mathcal{R} \sim 1300$ (Decaux *et al.* 1995), in the L-shell ions requires $\mathcal{R} \sim 200$ (Decaux *et al.* 1997), formally well outside the range of a CCD spectrometer.

A somewhat novel (for X-ray astrophysics) diagnostic is associated with the sensitivity of the energy levels to the chemical and physical state. The energy of the Kα transition in the neutral species shifts by small amounts depending on whether an atom is isolated or bound in a solid, and on the kind of solid. These effects are easy to see in the low-Z elements, and of course much harder to observe in Fe, whose K-shell doesn't care about what happens in the valence shell. As an example, the energy of the O K edge is at 545.4 eV for oxygen in the gas phase, and at 532.0 eV in oxides (Sevier 1979), and this difference shows up at modest resolving powers ($\mathcal{R} \sim 40$). Similarly, the energy of the Kα line shifts by ~ 4 eV, detectable at $\mathcal{R} \sim 130$. The corresponding numbers for Fe are $\mathcal{R} \sim 650$ to see the shift of the K edge, and ten times higher to detect any effect on the K$\alpha_{1,2}$ lines. Solid state and chemical bond effects will also broaden energy levels, with representative relative broadenings being of order $E/\Delta E \sim 1000$ for the K lines of the mid-Z elements (*e.g.* Citrin *et al.* 1974), and much larger for the lighter elements of course. These effects already showed up routinely in the ground calibration of the RGS. Fluorescent Fe K emission is of course well attested in astrophysical sources, and lower-Z fluorescence has already been seen with *ASCA* in a few sources (*e.g.* NGC 6552, Fukazawa *et al.* 1994; Reynolds *et al.* 1994).

EXAFS Spectroscopy In this context we also mention the curious EXAFS (Extended X-ray Absorption Fine Structure) effect, which manifests itself as a slow modulation of the photoelectric absorption cross section just above an absorption edge, in a solid (or any other material with short-range order). At photon energies just above the ionization energy, the photoelectrons have large de Broglie wavelengths, comparable to the lattice spacing of the solid. Hence, strong interference of the outgoing photoelectron wavefunction, with the wavefunction scattered by

neighboring atoms, takes place, which modulates the photoionization transition probability. Resonances occur approximately at photon energies $E_n \sim \chi + h^2n^2/8m_ea^2$ (from the interference condition $2ka = 2n\pi$, with $k = p/\hbar$ the photoelectron wavevector, a the lattice period or interatomic distance of the absorbing material, χ the ionization potential), so the effect becomes detectable already at moderate resolving powers of $\mathcal{R} \sim \chi/\Delta E = 25(\chi/1 \text{ keV})(a/1 \text{ Å})^2$. High signal-to-noise EXAFS spectra would allow one in principle to study the crystallography of interstellar dust, but already the mere detection of the effect may be of interest, to establish the presence of dust in certain absorbers (*e.g.* the absorbing material in type 2 AGN's). For a complete quantitative description of the effect, see Lee *et al.* (1981); astrophysical implications are discussed by Martin (1970), Evans (1986), and Woo (1995); and Owens *et al.* (1997) discuss the effect in the context of instrument calibration.

Excitation Mechanism The emission spectra of collisionally ionized gas and photoionized gas are radically different. Line emission in the former is mainly produced by radiative decays following direct collisonal excitation, while in the latter case, recombination and radiative cascades drive the line emission (Liedahl *et al.* 1990; for an introduction to spectral formation in photoionized plasmas we refer to Liedahl 1998). Electron temperatures in collisionally ionized gas are necessarily of order the ionization potentials, *i.e.* in the keV range for X-ray plasmas. Gas in photoionization and thermal equilibrium, of comparable mean ionization, however, is generally much cooler ($kT \ll \chi$; typical values are $kT \sim 10 - 100$ eV); or stated another way, photoionized gas is overionized with respect to the electron temperature (Liedahl 1998). This circumstance gives rise to a very distinctive signature of photoionization, namely, very narrow radiative recombination continuum (RRC) spectra. The monochromatic emissivity in the recombination continua is proportional to $vf(v)\sigma(v)dv/dE$, with v the electron velocity, $\sigma(v)$ the recombination cross section, $f(v)$ the the electron velocity distribution function, and E the photon energy (connected to v by energy conservation, $\frac{1}{2}mv^2 + \chi = E$). In hot gas, $f(v)$ is broad, and the continua are consequently broad and of low amplitude. In cool, photoionized gas, however, the RRC's are narrow because the electron velocity distribution is narrow. The spectra show as sharp emission edges, with a narrow ($\Delta E \sim kT \ll \chi$) roughly exponential decay. In fact, since the width of the features is approximately $\Delta E \sim kT$, they provide a straightforward temperature diagnostic. In H-like ions, the total flux in the RRC is of the same order as the flux in Lyα, and the features are easily visible. To detect this signature of photoionization, one needs to be able at least to resolve Lyα from the $n = 1$ ionization energy, which requires resolving power $\mathcal{R} > 4$ (and a similar requirement for the He-like ions); more realistically, to avoid confusion of the RRC with Lyβ and the closely spaced higher series members requires $\mathcal{R} > 9$. To measure electron temperatures from the width of the RRC's requires energy resolution $\Delta E \sim kT_e$, which may be as low as 10 eV. The perfect astrophysical example is the *ASCA* spectrum of the massive binary Cyg X-3, which shows a complete, optically thin recombination spectrum. We evidently see emission from a photoionized wind flowing off the companion Wolf-Rayet star, ionized by hard emission produced close to the compact object (Liedahl and Paerels 1996).

For the Fe L ions, the line emission spectra are also very different in collisional and radiation driven plasmas (Liedahl *et al.* 1990), a consequence of the fact that radiative recombination, and the ensuing cascades, preferentially populate upper levels different from those populated by direct collisional excitation. This is shown in Figure 2, taken from Liedahl *et al.* (1990). It takes resolving power $\mathcal{R} \sim$ a few tens to detect the difference. In this example, note the bright line near 15 Å—the brightest line near this wavelength actually arises in a different ion depending on the excitation mechanism. This implies that there may be a coupling between the assignment of line identifications and the emission mechanism (depending on wavelength resolution and accuracy of the wavelength scale), which has implications for attempts to automate the identification process.

These two emission mechanisms, collisional excitation and recombination, are the two simplest, extreme cases, and both are well studied. In practice, temperatures in photoionized gas may be high enough that a complete radiative/collisional model has to be devised. And of course radiative transfer effects (*e.g.* scattering off resonance lines) may further complicate the issue.
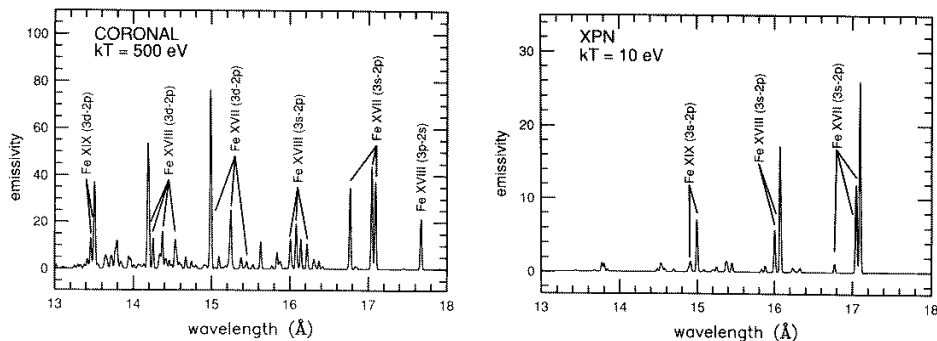

Fig. 2.— Emission line spectra from selected Fe L ions under conditions of collisional ionization equilibrium (*left*), and photoionization equilibrium (*right*) (from Liedahl *et al.* 1990).

Density Diagnostics: He-like Ions The He-like ions provide a well-known, relatively easy to apply density diagnostic (Gabriel and Jordan 1969; Mewe 1998). Three $n = 2 \rightarrow 1$ transitions make up the characteristic He-like 'triplets', a resonance line ($1s^2\ ^1S - 1s2p\ ^1P$), an intercombination line ($1s^2\ ^1S - 1s2p\ ^3P$, actually two very closely spaced lines), and a forbidden line ($1s^2\ ^1S - 1s2p\ ^3S$). At very low densities, excitation to any of these levels is followed by spontaneous radiative decay, but at higher densities, the collisional rate from the upper level of the forbidden line to that of the intercombination line starts to compete with the spontaneous rate. The result is a brightening of the intercombination line at the expense of the forbidden line, and the ratio between the forbidden and intercombination line is a density diagnostic. The population kinetics between the lowest levels is approximately the same for collisional excitation and for the recombination dominated case, so the diagnostic works approximately the same in collisional and photoionized plasmas. The density at which the collisional and radiative rates out of the upper level of the forbidden line are (roughly) equal is defined as the critical density for the ion. At very high densities, the

forbidden line is essentially suppressed, and the spectrum is effectively insensitive to density again. Therefore, the spectrum has optimum density sensitivity in a range around the critical density. Since the critical density depends on atomic structure, it depends on nuclear charge (and very strongly so, approximately as Z^{13}; Mewe 1998). With the He-like spectra of O through Si in the RGS band, this provides sensivity to densities in the range $10^{10} - 10^{16}$ cm^{-3}. To use the diagnostic, one needs to be able to separate the intercombination and forbidden lines, which requires resolving power $\mathcal{R} \sim 70 - 250$ (O through Fe).

Density Diagnostics: Fe L Ions The Fe L ions provide another density diagnostic. Both in collisionally and photoionized plasmas, metastable levels in the $n = 2$ shell develop a finite population with increasing density (Mason *et al.* 1979; Mewe *et al.* 1985, 1991; Liedahl *et al.* 1992). These excited ions provide additional sources for collisional or recombination driven emission, with spectra that are different from those produced by the ground state ions. The net result is roughly that the total line flux per ion remains approximately the same, but is distributed over a larger number of transitions—the spectra become more complex. A good example is provided by Figure 4 in Liedahl *et al.* (1992), which gives model coronal and recombination-driven spectra for Fe XX, for low and high densities. Once again, there is a critical density for this process, which ranges from $\sim 10^{10} - 10^{15}$ cm^{-3}. Ideally, one would look specifically for the presence or absence of the strongest lines that appear at high density, but this requires rather high resolving power (typically $\mathcal{R} \gtrsim 100$ – few hundred). With sufficient sensitivity, it may be possible to detect the increasing complexity of the spectrum with increasing density even if transitions can not be individually resolved, through the redistribution of broad-band line power in the Fe L band.

Most of the above diagnostics are summarized in Figure 3 (along with other standard diagnostics that are not accessible with the RGS), along with the resolving power (in the FWHM sense) of the RGS.

3. Qualitatitive Spectroscopy: Inferring Emission Mechanisms and Source Conditions from the Spectroscopic Data

With the aid of some of the above diagnostics, one can examine an observed spectrum, and in principle obtain a qualitative assessment of the source characteristics, which guides the choice of an appropriate spectral model. As has been argued above, mere line identifications are not likely to be very effective in this process. Rather, already at this stage one can exploit the powerful principle of spectroscopic consistency: each transition is accompanied by other transitions arising in the same ion, and rather than ID'ing lines, one could attempt to ID entire ionic spectra.

As a starting point, one may simply look for the strongest transitions in each ion likely to be present. Each ion only has a few strong lines, and listing these will also give some idea of the extent to which a typical RGS spectrum is likely to be crowded. The strongest lines in the H- and He-like ions of O through Si, and the strongest lines in the eight Fe L ions (in collisional
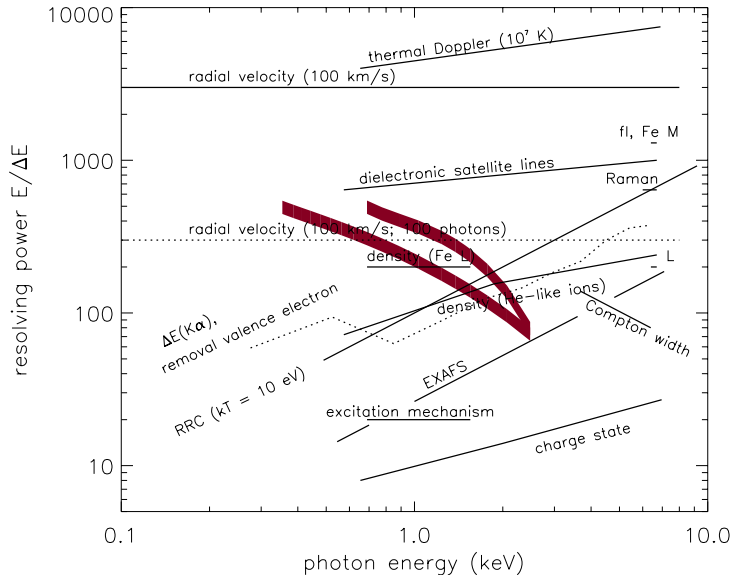
Fig. 3.— Resolving power for several spectroscopic diagnostics, along with the resolving power in orders $m = -1, -2$ of the RGS (*red bands*). 'Charge state' refers to the resolving power required to distinguish the H- and He-like spectra; 'excitation mechanism' refers to resolving power required to detect the difference between the collisional and the recombination Fe L spectra. Possible diagnostics not discussed here are either at high energy (Compton recoil width at Fe K, Raman-scattered Fe K, dependence of the Fe Kα line energy on charge state for the M and L-shell ions, marked 'fl, Fe M' and 'L', respectively), or require very high resolving power (dielectronic satellite spectroscopy, thermal Doppler broadening) (See Paerels 1998 and references therein).

equilibrium) are listed in Table 1; convolved with a $\Delta\lambda = 0.08$ Å FWHM Gaussian (a very rough approximation to the RGS response), they are displayed in Figure 4. As is evident from the plot, this is a manageable set (reassuring remarks courtesy Duane Liedahl (1997)).

4. Quantitative Spectroscopy: Analysis of Real Data

Finally, two remarks on practical, quantitative analysis of RGS data. The RGS is read out with dedicated CCD camera's, and for each event we get both the position in the focal plane, and the CCD pulse height. A particularly powerful representation of the data results if one integrates the spectrum over a mask in the cross-dispersion direction, and plots events in the dispersion/pulse height plane. Figure 5 shows a raw calibration spectrum in this representation, obtained with RGS1 at MPE's Panter X-ray calibration facility (see also Brinkman *et al.* and Rasmussen *et al.*, these proceedings). The X-ray source was an electron impact source with a Si anode. Events have been reconstructed, but no attempt has been made to place the CCD pulse heights on a common scale; hence, the spectrum shows small discontinuities at the eight CCD chip boundaries. A schematic of this plot is shown in Figure 6, for reference. In Figure 5 and 6,

Table 1: The Thirty Strongest Transitions Likely
to Dominate Most RGS Spectra

Element	Ion	wavelength (Å)
O	O VII	21.60, 21.80, 22.10
	O VIII	18.97
Ne	Ne IX	13.44, 13.55, 13.70
	Ne X	12.13
Mg	Mg XI	9.17, 9.23, 9.31
	Mg XII	8.42
Si	Si XIII	6.65, 6.69, 6.74
	Si XIV	6.18
Fe	Fe XVII	15.01, 16.78, 17.05, 17.10
	Fe XVIII	14.20
	Fe XIX	13.52
	Fe XX	12.83
	Fe XXI	12.29
	Fe XXII	11.77
	Fe XXIII	11.41, 11.74, 12.19
	Fe XXIV	10.65, 11.18

the right hand side of the plots corresponds approximately to $\lambda 5$Å, the left hand side to $\lambda 35$Å. The dispersion coordinate, Δz, is in CCD pixels. This coordinate is approximately proportional to the arc length, ℓ, along the Rowland circle between the telescope and spectroscopic foci (see Brinkman et $al.$, these proceedings, Fig.1, for the geometry), and this arc length is proportional to the dispersion angle β: $\ell = 2R(\alpha + \beta)$, with R the radius of the Rowland circle, α the angle of incidence on the gratings; α and β are the angles between the plane of the grating and the incident and disprsed rays, respectively. Wavelength, angle of incidence, and dispersion angle are related by the dispersion relation for the reflection gratings:

$$\cos\beta = \cos\alpha + m\lambda/d, \qquad (1)$$

with m the spectral order number, and d the (mean) grating period. The bright, curved bands (hence the informal name 'banana plot' for this representation of RGS spectra) are the bremsstrahlung continuum spectrum from the source; the curvature is of course due to the inverse relation between photon energy and photon wavelength. Several orders $m = -1, -2, -3, -4$ are visible, when photons detected at a given position on the CCD camera are split up according to their pulse heights (vertical, constant offsets for a given dispersion angle).

Strong Si K (in 4 spectral orders) and O K (near the botttom of the plot) emission lines can be seen, as well as a deep absorption edge due to the Co beam filter. The asterisks in Figure
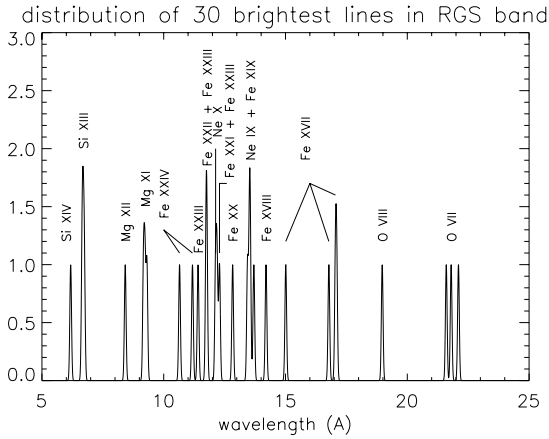
Fig. 4.— Distribution of the thirty transitions in Table 1. The lines have been convolved with a $\Delta\lambda = 0.08$ Å FWHM Gaussian profile.

6 mark the response to a single physical emission line (Si K). In between the various orders of the line, one sees a faint band of light scattered by microroughness on the gratings (single pulse height, range in dispersion angle, hence a horizontal band, represented by the horizontal dotted line in Figure 6). The advantage of this representation of the data is clear: it allows a separation of scattered light from strong emission lines, and true continuum radiation.

The response of the CCD detectors appears in the vertical direction. Between the bright photopeak (at pulse height corresponding to Si Kα, or $E \approx 1740$ eV) and pulse height zero, one sees the 'tail' of partially collected charge (vertical dotted lines in Figure 6; Si Kα photons with partially collected charge appear at the dispersion angles for Si Kα, but are spread out in CCD pulse height), which contains a few percent of the total flux in the line. Also in the vertical direction, we see 'piled-up' events at twice the Si Kα pulse height, each with their own partial charge collection tail (only in the brightest orders).

The characteristic 'cross' shaped response to monochromatic radiation in the dispersion/pulse height diagram may be the basis for the most sensitive line detection algorithm, by cross-correlating this response with real data, using all the know spatial/ pulse height response information in the search.

The banana plots immediately visualize another systematic effect. The CCD partial charge collection tail of a strong higher order emission line may cross the lower order continuum spectra (as happens at the spot marked 'A' in Figure 6). Were one to extract a first order spectrum by putting a banana-shaped mask on Figure 6 centered (in pulse height) on the first order continuum, an artificial discrete feature would appear in this 'first order spectrum' at the dispersion coordinate corresponding to point 'A'— which is not a real first order emission line. Where this might happen in a given dataset is immediately obvious from looking at the data this way; and for certain datasets, one may wish to model the data in this same space, instead of in the traditional 1D

spectral space. As a final example, if there are multiple sources in the field of view, offset along the dispersion direction, the best way to inspect and analyze the data, and to take into account the spectral 'cross-talk' between the sources, is to work in dispersion/pulse height space.

From these examples, it should be clear that the additional information provided by the CCD pulse height offers a powerful way to visualize and interpret data, which goes far beyond mere 'separation of orders'—an advantage provided by "reading out a spectrometer with a spectrometer" (F. Jansen, 1993, [priv. comm.]).

As a final example of how one could deal with apparent systematics in the data, we briefly discuss the issue of the wavelength scale for the RGS. The zero order image does not fall on the detector. Based on the known geometry, and its response to a changing thermal environment, and the known pointing direction of the telescope, the wavelength scale can be derived, and this procedure will be calibrated in orbit using a number of strong emission line point sources (assuming the wavelengths in the astrophysical source are known!). It is important to realize that this a highly constrained procedure; conversely, if any systematic wavelength shifts appear in your data, it's easy to check whether these could be due to a small systematic error in your wavelength scale. The starting point for such an analysis is always the dispersion equation, Eq.(1). Every systematic distortion to the wavelength scale due to a physical effect has its own wavelength signature. As an example, suppose there is a small systematic error on the pointing position (or the source position !) with respect to the position assumed in the derivation of the default wavelength scale. Taking the differential of Eq.(1), we find

$$\Delta\lambda = \frac{d}{m}\sin\alpha\Delta\alpha \tag{2}$$

with $\Delta\alpha$ the change in the incidence angle on the gratings due to the offset in pointing. This effect produces *constant* wavelength residuals, characterized by a single parameter $\Delta\alpha$. Another example is the perturbation introduced by a linear offset Δz_0 of the detector along the dispersion direction. Such an offset might be the result of an uncalibrated small amount of bending of the telescope tube. A linear shift Δz_0 corresponds to an angular shift $\Delta\beta \approx \Delta z_0/L$, with L the distance between the center of the grating array and the spectroscopic focus (approximately constant along the detector). Using the dispersion relation, we find

$$\sin\beta\Delta\beta = m\Delta\lambda/d, \tag{3}$$

from which we obtain the wavelength residual:

$$\Delta\lambda = \frac{d}{m}\frac{\Delta z_0}{L}\sin\beta \tag{4}$$

which has a strong wavelength dependence, with a single free parameter, Δz_0. Similar considerations hold for other physical perturbations; perturbations to the wavelength scale can therefore be diagnosed and corrected using a simple physical model for the spectrometer, and a small number of free parameters.

5.   Conclusion

High resolution spectroscopy with *XMM* will bring a powerful array of spectroscopic diagnostics within reach, with obvious implications for the astrophysics of all classes of cosmic X-ray source. In order to fully utilize the high information content of spectroscopic data from the RGS, novel ways of data analysis, visualization, and extraction of quantitative physical information will have to be developed, which explicitly take into account atomic physics, astrophysics, and the physics of the instruments—not unlike the case with astrophysical spectroscopy in other wavelength bands.

REFERENCES

Brown, G. V., Beiersdorfer, P., Liedahl, D. A., Widmann, K., & Kahn, S. M. 1998, ApJ, 502, 1015.

Decaux, V., Beiersdorfer, P., Osterheld, A., Chen, M., & Kahn, S. M. 1995, ApJ, 443, 464.

Decaux, V., Beiersdorfer, P., Kahn, S. M., & Jacobs, V. L. 1997, ApJ, 482, 1076.

Citrin, P. H., Eisenberger, P. M., Marra, W. C., Åberg, T., Utriainen, J., & Källne, E. 1974, Phys. Rev. B, 10, 1762.

Evans, A. 1986, MNRAS, 223, 219.

Fabian, A. C., Arnaud, K. A., Bautz, M. W., & Tawara, Y. 1994, ApJ, 436, L63.

Fukazawa, Y., et al. 1994, PASJ, 46, L141.

Gabriel, A. H., & Jordan, C. 1969, MNRAS, 145, 241.

Kaastra, J., & Mewe, R. 1993, A&AS, 97, 443.

Lee, P. A., Citrin, P. H., Eisenberger, P. and Kincaid, B. M. 1981, Rev. Mod. Phys., 53, 769.

Liedahl, D. A. 1998, in *X-ray Spectroscopy*, J. van Paradijs (ed.), (Springer: Heidelberg).

Liedahl, D. A., Kahn, S. M., Osterheld, A. L., and Goldstein, W. H. 1990, ApJ, 350, L37.

Liedahl, D. A., Kahn, S. M., Osterheld, A. L., & Goldstein, W. H. 1992, ApJ, 391, 306

Liedahl, D. A., Osterheld, A. L., & Goldstein, W. H. 1995, ApJ, 438, L115.

Liedahl, D. A., & Paerels, F. 1996, ApJ, 468, L33.

Martin, P. G. 1970, MNRAS, 149, 221.

Mason, H. E., Doschek, G. A., Feldman, U., & Bhatia, A. K. 1979, A& A, 73, 74.

Mewe, R., Gronenschild, E. & van den Oord, G. 1985, A& AS, 62, 197.

Mewe, R. 1991, A& AR, 3, 127.

Mewe, R., Kaastra, J. S., Schrijver, C. J., van den Oord, G. H. J., and Alkemade, F. J. M. 1995, A&A, 296, 477.

Mewe, R. 1998, in *X-ray Spectroscopy*, J. van Paradijs (ed.), (Springer: Heidelberg).

Reynolds, C.S., Fabian, A.C., Makishima, K., Fukazawa, Y., & Tamura, T. 1994, MNRAS, 268, L55.

Owens, A., Denby, M., Wells, A., Keay, A., Graessle, D. E., and Blake, R. L. 1997, ApJ, 476, 924.

Paerels, F. 1998, in *X-ray Spectroscopy*, J. van Paradijs (ed.), (Springer: Heidelberg).

Schmitt, J. H. M. M., Drake, J. J., & Stern, R. A. 1996, ApJ, 465, L51.

Schrijver, C. J., van den Oord, G. H. J., & Mewe, R. 1994, A&A, 289, L23.

Sevier, K. D. 1979, Atomic Data and Nuclear Data Tables, 24, 323.
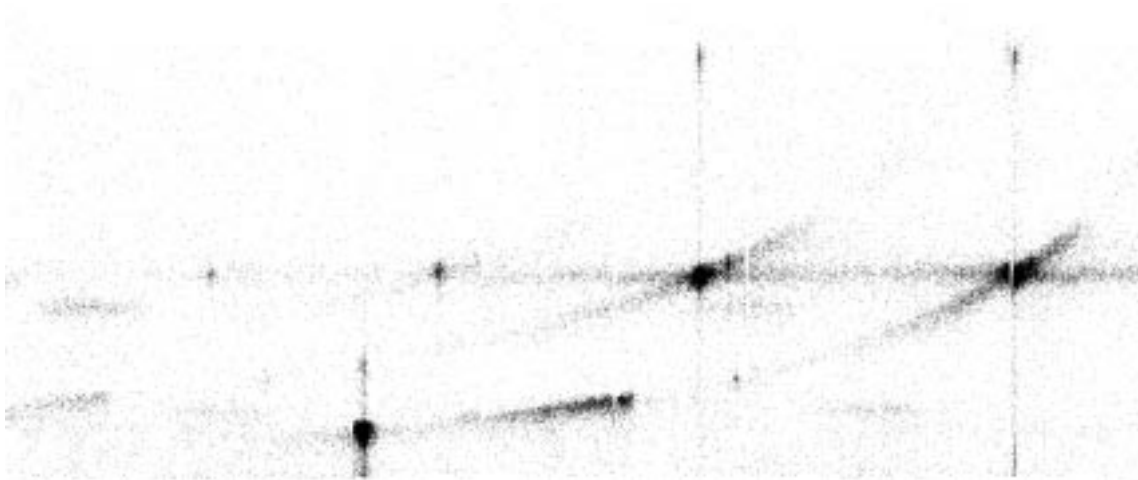
Woo, J. W. 1995, ApJ, 447, L129.

Fig. 5.— A SiO calibration spectrum, obtained with RGS1, in dispersion/pulse height representation. Dispersion runs horizontally, between 5 Å at the right, to 35Å at the left; the coordinate is in 27 μm CCD pixels. Vertical coordinate is CCD pulse height, in ADU (0 through 4095, approximately corresponding to photon energies 0–3700 eV, bottom to top).
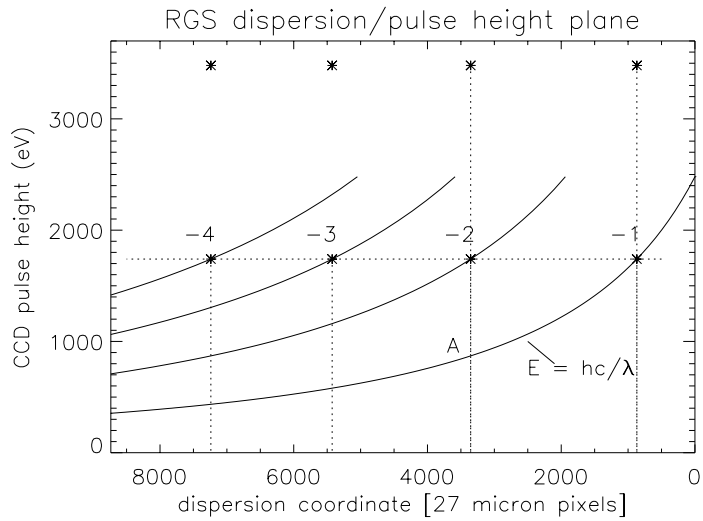

Fig. 6.— A schematic of the dispersion/pulse height plane for the calibration spectrum shown in Figure 5.